remote sensing

MDPI

Article

Passive L-Band Microwave Remote Sensing of Organic Soil Surface Layers: A Tower-Based Experiment

François Jonard [1,2,*], Simone Bircher [3], François Demontoux [4], Lutz Weihermüller [1], Stephen Razafindratsima [4], Jean-Pierre Wigneron [5] and Harry Vereecken [1]

1 Agrosphere (IBG-3), Institute of Bio- and Geosciences, Forschungszentrum Jülich GmbH, 52428 Jülich, Germany; l.weihermueller@fz-juelich.de (L.W.); h.vereecken@fz-juelich.de (H.V.)
2 Earth and Life Institute, Université catholique de Louvain, 1348 Louvain-la-Neuve, Belgium
3 CESBIO, Université de Toulouse, CNES/CNRS/IRD/UPS, 31400 Toulouse, France; simone.bircher@cesbio.cnes.fr
4 IMS Laboratory, Université de Bordeaux, 33607 Pessac, France; francois.demontoux@u-bordeaux.fr (F.D.); stephen.razafindratsima@u-bordeaux.fr (S.R.)
5 INRA, Centre INRA Bordeaux Aquitaine, URM1391 ISPA, 33140 Villenave d'Ornon, France; jpwigner@bordeaux.inra.fr
* Correspondence: f.jonard@fz-juelich.de; Tel.: +49-2461-61-9518

Received: 30 November 2017; Accepted: 7 February 2018; Published: 16 February 2018

Abstract: Organic soils play a key role in global warming because they store large amount of soil carbon which might be degraded with changing soil temperatures or soil water contents. There is thus a strong need to monitor these soils and, in particular, their hydrological characteristics using, for instance, space-borne L-band brightness temperature observations. However, there are still open issues with respect to soil moisture retrieval techniques over organic soils. In view of this, organic soil blocks with their vegetation cover were collected from a heathland in the Skjern River catchment in western Denmark and then transported to a remote sensing field laboratory in Germany where their structure was reconstituted. The controlled conditions at this field laboratory made it possible to perform tower-based L-band radiometer measurements of the soils over a period of two months. Brightness temperature data were inverted using a radiative transfer (RT) model for estimating the time variations in the soil dielectric permittivity and the vegetation optical depth. In addition, the effective vegetation scattering albedo parameter of the RT model was retrieved based on a two-step inversion approach. The remote estimations of the dielectric permittivity were compared to in situ measurements. The results indicated that the radiometer-derived dielectric permittivities were significantly correlated with the in situ measurements, but their values were systematically lower compared to the in situ ones. This could be explained by the difference between the operating frequency of the L-band radiometer (1.4 GHz) and that of the in situ sensors (70 MHz). The effective vegetation scattering albedo parameter was found to be polarization dependent. While the scattering effect within the vegetation could be neglected at horizontal polarization, it was found to be important at vertical polarization. The vegetation optical depth estimated values over time oscillated between 0.10 and 0.19 with a mean value of 0.13. This study provides further insights into the characterization of the L-band brightness temperature signatures of organic soil surface layers and, in particular, into the parametrization of the RT model for these specific soils. Therefore, the results of this study are expected to improve the performance of space-borne remote sensing soil moisture products over areas dominated by organic soils.

Keywords: L-band radiometry; microwave remote sensing; organic soil; soil dielectric permittivity; soil moisture; inverse modelling; tower-based experiment

1. Introduction

Hydrological states of the land surface affect energy and matter fluxes between the atmosphere and the land surface. Global information on these transfer processes is highly relevant to improving predictions of weather and environmental disasters and, in general, to advancing research on climate change. Organic soils, typical of the northern cold climate zone, are known to be sensitive to global warming due to increased losses of soil carbon with increasing temperatures to both the atmosphere in the form of greenhouse gases and in a dissolved state to the hydrosphere [1,2]. Additionally, soil moisture plays a key role in determining the rate of soil carbon cycling and the type of carbon emission (e.g., [3,4]). There is thus a strong need to monitor these soils and, in particular, their hydrological characteristics in order to better understand the processes that link the terrestrial water and carbon cycles in these climate-sensitive northern regions.

Space-borne remote sensing techniques are particularly well adapted to globally monitor dynamic processes on the Earth's surface. During the last decade, significant progress has been made in the development of satellite-based instruments for hydrological applications [5]. Thus far, three innovative space missions with passive L-band (1–2 GHz corresponding to vacuum wavelengths of 30–15 cm) microwave instruments aboard have been launched, with the objective to provide frequent-revisit global mapping of surface soil moisture. The European Space Agency (ESA) Soil Moisture and Ocean Salinity (SMOS) satellite launched in 2009 was the first L-band radiometer mission [6], followed by the U.S. National Aeronautics and Space Administration (NASA) and Argentinean Space Agency (CONAE) Aquarius/Satélite de Aplicaciones Científicas (SAC)-D mission in 2011 (and stopped in 2015) [7], and the NASA Soil Moisture Active Passive (SMAP) satellite launched in 2015 [8].

In addition to soil moisture retrieval at global scale, these new space missions provide opportunities for improved understanding and monitoring of plant water status. Indeed, the thermal radiance, also called brightness temperature, emitted from the soil surface and measured by the L-band radiometer is affected by attenuation through the vegetation canopy. This attenuation, referred to as vegetation optical depth, is proportional to the vegetation water content, and, therefore, might be used to get insight into plant water status, plant growth, plant health, and consequently into the processes linking the water and carbon cycles [9,10].

Compared to higher microwave frequency bands used in the past (C-, X-, and K-bands), the L-band frequency range has several advantages for soil moisture monitoring. The soil emission depth at L-band is larger, which makes it possible to obtain information not only from the top surface but also through the first few centimetres of the soil. Additionally, the frequency range 1.400–1.427 GHz within the L-band is protected, which means that the brightness temperatures at these frequencies are less affected by man-made radio frequency interferences (RFI). Sensors operating at lower frequencies (UHF or P-band) could also be used to obtain information deeper into the soil. Nevertheless, the required antenna size (increasing with increasing wavelength) and the large presence of RFI make it difficult to use these sensors for space-borne remote sensing. Finally, compared to optical measurements, microwave observations can be performed at almost any time because the atmosphere and clouds are largely transparent to microwave radiations and the observations are independent of solar radiation.

The brightness temperature signatures measured at microwave frequency are not only dependent on soil and vegetation water content but also on soil surface roughness and organic matter content. Many researchers have already investigated the effect of soil surface roughness on microwave signals [11,12]. During recent years, the effect of soil organic matter on passive L-band microwave signals has also been studied in the context of the ESA SMOSHiLat project [13]. L-band radiometer algorithms for soil moisture retrieval are based on the use of a radiative transfer (RT) model [12,14,15] and a dielectric mixing model [16–18] to derive soil moisture information from brightness temperature observations. The listed dielectric mixing models were developed for mineral soils and no information on organic matter content can be accounted for. However, organic soils are known to exhibits specific hydrological characteristics such as high porosity and low bulk density, high water holding capacity and bound water fractions due to their complex structure with large specific surface areas, as well

as a higher potential for water infiltration because of the macropores created by the organic matter. For this reason, dielectric mixing models were recently also developed for organic soil layers [19–22]. The empirical model proposed by Bircher et al. [19] is currently being implemented in the SMOS soil moisture retrieval algorithm to replace the Mironov et al. [17] model wherever organic soil surface layers are present. Calibrated on a wide range of organic substrate types over the entire wetness range and not requiring any auxiliary input that may be difficult to obtain globally, this model is suitable for such global applications. However, there are still open issues with respect to such soil moisture retrieval techniques from passive L-band observations over organic soil surfaces. For example, the roughness and vegetation parameters applied in the RT equations should be specifically calibrated over organic soil surfaces.

The objective of this study is to evaluate experimentally the possibility of retrieving the dielectric permittivity of organic soils from ground-based passive L-band microwave remote sensing data. A further motivation is to derive specific soil roughness and vegetation parameters for organic soil surfaces, which could be used to improve the space-borne passive microwave soil moisture products acquired above such surfaces. To this end, organic soils collected from a heathland in the Skjern River catchment in western Denmark were monitored over a period of two months using a tower-based L-band radiometer. Brightness temperature data were inverted to derive the time variations in the soil relative dielectric permittivity. It must be noted that relative dielectric permittivity is a complex value. In this study, the relative dielectric permittivity denomination (ε_r) refers to its real part. The remote estimations of the relative dielectric permittivity were finally compared to in situ measurements.

2. Materials and Methods

2.1. Experimental Setup

Organic soils with their vegetation cover were collected from a heathland located in the Gludsted plantation in the Skjern River catchment in western Denmark (latitude 56°04′19″ N, longitude 9°17′39″ E). The test site has been intensively investigated in the framework of the Danish Hydrological Observatory (HOBE, www.hobecenter.dk).

The soil type is podzol of coarse sandy texture (85% sand, 14% silt, and 1% clay content) with a pronounced organic surface layer. Figure 1 illustrates the corresponding soil profile in form of a photo as well as a detailed and simplified scheme. The organic layer is classified as moder with all horizons OL–OF–OH present, although with a less pronounced semi-decomposed (OF) part. The OH horizon is intermixed with sand lenses below a certain depth. To the naked eye, it is difficult to discern the OH horizon from the underlying mineral Ah horizon as the latter still contains a substantial organic fraction (16% organic matter). Only a consistency change (from very slimy/sticky to more grainy/loose) and a significant drop in ThetaProbe wetness measurements (not shown) from the organic to the mineral sandy layer gave clear indications in that respect. The vegetation above the soil is mainly composed of moss, scotch heather, crow berry, cranberry, and grasses.

Forty blocks of undisturbed soil–vegetation were excavated in August 2013 and carefully transported in four wooden boxes to the Selhausen experimental test site, which is part of the Terrestrial Environmental Observatories (TERENO, www.tereno.net) network in Germany (Figure 2). Each block had an area of about 60 cm by 70 cm totalling an area of approximately 17 m^2 of soil. The thickness of the soil layers (organic + mineral layers) was 13–15 cm and the height of the vegetation was around 15–20 cm (Figure 1).

To characterize the L-band emissions of the organic soil surface layers and their vegetation cover, the field laboratory for ground-based remote sensing developed by Jonard et al. [23] at the Selhausen test site (Germany) was used (Figure 3). This field laboratory offers the unique possibility of highly controlled acquisitions of microwave remote sensing data accompanied by the essential in situ soil and vegetation data such as temperature and moisture profiles. It includes an L-band radiometer installed at 4 m height with a fixed incidence angle of about 36° to measure time series of brightness

temperature at horizontal (H) and vertical (V) polarizations. The radiometer is directed towards a 2 m × 2 m box filled with sand down to a depth of 1 m. To increase the sensitivity of the radiometer measurements to radiance originating from the sand box and to minimize the influence of radiance from the surrounding area, a wire grid with a mesh size of 0.5 cm was placed around the sand box. A complete description of the setup is available in [23].

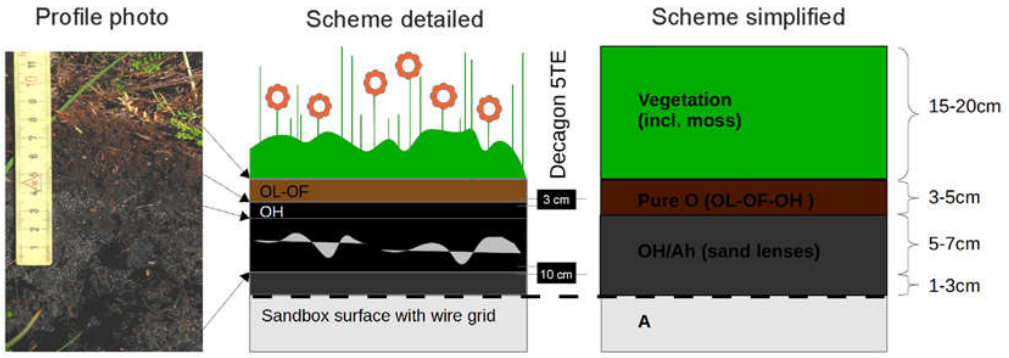

Figure 1. Photo (**left**) as well as detailed (**middle**) and simplified (**right**) scheme of vegetation–soil profile as encountered at the HOBE site in the Gludsted heathland, Denmark, and reinstalled at the Selhausen remote sensing field laboratory in Germany, on top of the sandbox surface covered with a wire grid.

Figure 2. Undisturbed soil–vegetation blocks excavated using a hydraulic excavator from the HOBE heathland test site in the Skjern River catchment, Denmark (**left**), and transported in wooden boxes (**right**) to the Selhausen remote sensing field laboratory in Germany .

Figure 3. The Selhausen remote sensing field laboratory (Germany) consisting of an L-band radiometer (yellow box + conical horn antenna) fixed at 4 m height on an aluminium arc and a sand box covered by the soil–vegetation blocks in the centre of a wire grid.

Several undisturbed soil–vegetation blocks from the HOBE test site were placed together on top of the sand box and cut to exactly cover the 2 m × 2 m area. Below the soil, a horizontal metal sheet was installed to control the bottom boundary condition in the microwave emission model. As a result, regions underneath this metal sheet have no influence on the measured brightness temperature. Outside the radiometer footprint, a second area of 2 m × 2 m covered with additional soil–vegetation blocks was installed to get a reference observation area for destructive soil and vegetation samplings. Time-lapse radiometer observations were then carried out over two months, from the 2 October (DOY 275) to the 26 November (DOY 330) 2013, to collect time series of brightness temperature at different soil–vegetation moisture conditions. The soil in the sandbox within the radiometer footprint as well as the reference plot were watered (about 300 L per plot) on 8 October (DOY 281). The measurements were performed under natural drying and wetting conditions. Unfortunately, frequent rain events kept the soil water content quite constant over the experimental duration.

At the end of the measurement period, a three-day experiment was carried out, in which the surface vegetation and soil layers were removed sequentially (i.e., Step 2 and Step 3 in Figure 4: vegetation layer removed first and then organic layer removed) and put back on with a wire grid between each layer (i.e., Step 4 and Step 5: organic soil layer alone, then vegetation layer alone on a wire grid), and finally the vegetation and organic layers together on a wire grid (Step 6) in order to acquire radiometer measurements of each layer separately as well as all combinations of the layers.

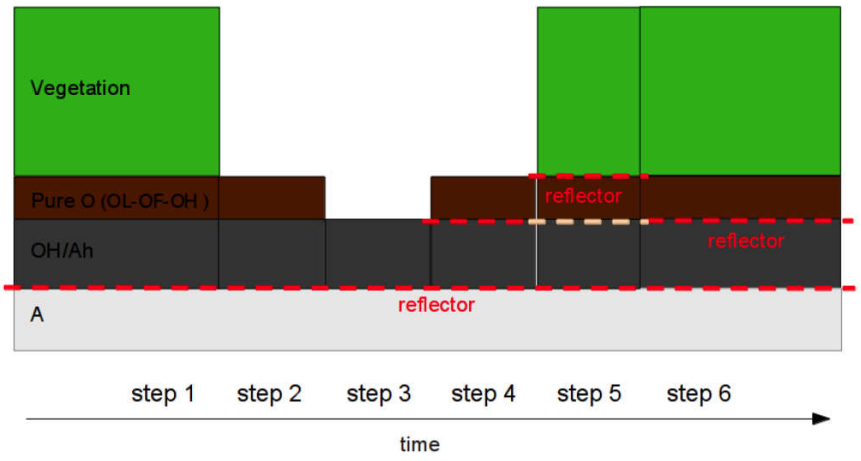

Figure 4. Sketch of the different measurement configurations during the layer experiment.

Simultaneously with the L-band observations, soil relative dielectric permittivity, soil temperature, and soil bulk electrical conductivity data were recorded using capacitance sensors 5TE (Decagon Devices Inc., Pullman, WA, USA). The 5TE sensors were installed horizontally at two different depths (3 and 10 cm) in triplicates in the radiometer observation footprint as well as in the reference plot. Additional soil moisture measurements were carried out with a FDR (frequency domain reflectometry) sensor ThetaProbe ML2x (Delta-T Devices Ltd., Cambridge, UK) in both plots, whereby the sensor was inserted from the top down 6 cm. Furthermore, soil and vegetation samples were periodically collected from the reference plot to estimate the volumetric water content of the organic and mineral layers as well as the gravimetric water content of the vegetation. Soil samples were also used for laboratory measurements of physicochemical properties (texture, bulk density, and organic matter content). In addition, the destructive volumetric soil water content measurements were used to calibrate the in situ soil moisture sensors (see [24]).

2.2. L-Band Radiometer

L-band microwave remote sensing measurements were performed using an ELBARA II radiometer, which is a similar instrument to those used by the European Space Agency (ESA) for

ongoing SMOS validation and research activities. The ELBARA II measures brightness temperatures within the protected part, i.e., 1400–1427 MHz, of the microwave L-band. The radiometer was attached to a Pickett-horn antenna to perform measurement at H and V polarizations (Figure 3). The absolute accuracy of the brightness temperature measurements is better than ±1 K, and the sensitivity is < 0.1 K. Internal calibrations were performed before each measurement by using internal noise reference sources, i.e., a hot resistive noise source at about 313 K and an active cold source at about 40 K. The radiometer was also regularly calibrated by measuring sky radiance at an elevation angle of about 55° above the horizon and oriented approximately toward the north. Radiometer measurements were performed every 15 min during the two-month experiment.

2.3. Radiative Transfer Model

The brightness temperature or thermal radiance measured by the L-band radiometer (TB_p, K) at horizontal (p = H) and vertical (p = V) polarization can be expressed as the linear combination of the radiance emitted from the scene of interest ($TB_{S,p}$, K) and the radiance emitted from the surrounding area covered with the wire grid ($TB_{O,p}$, K), i.e.,

$$TB_p = \eta_p TB_{S,p} + (1 - \eta_p) TB_{O,p}, \quad (1)$$

where η_p and $(1 - \eta_p)$ are the fractional amounts of radiance emitted from the scene of interest and the surrounding area, respectively. The weighting factor η_p can be derived from TB_p measurements performed with the scene of interest (i.e., the sand box) covered with different surfaces with known reflectivities as described in [23] and using

$$TB_p = \eta_p[(1 - R_{s,p})T_s + R_{s,p}T_{sky}] + (1 - \eta_p)[(1 - R_{o,p})T_o + R_{o,p}T_{sky}], \quad (2)$$

where $R_{s,p}$ and $R_{o,p}$ are the reflectivities of the scene of interest and the surrounding area, respectively; T_s (K) and T_o (K) are the effective physical temperatures of the scene of interest and the surrounding area, respectively; and T_{sky} (K) is the sky brightness temperature ($T_{sky} \approx 4.8$ K).

A first set of 10 measurements was performed with the sand box covered with a reflector (wire grid), for which the reflectivity R_s is assumed to be 1. The mean values of the TB measurements obtained with this setup were 14.9 K and 14.3 K for the H and V polarization, respectively. A second set of 10 measurements was performed with the sand box covered with a microwave absorber (EPP22, Telemeter Elektronic, Donauwörth, Germany), for which R_s is assumed to be 0. In this case, the mean values of the TB measurements were 160.3 K and 166.3 K for the H and V polarization, respectively. Based on these specific assumptions for R_s, Equation (2) can be reduced to:

$$TB_p = \eta_p\, T_{sky} + (1 - \eta_p)[(1 - R_{o,p})T_o + R_{o,p}T_{sky}], \quad (3)$$

and

$$TB_p = \eta_p\, T_s + (1 - \eta_p)[(1 - R_{o,p})T_o + R_{o,p}T_{sky}], \quad (4)$$

for the L-band TB measurements with the sand box covered respectively with a reflector (Equation (3)) and an absorber (Equation (4)). Solving Equations (3) and (4) for the two unknowns (i.e., η_p and $R_{o,p}$) yielded $\eta_H = 0.52$, $\eta_V = 0.54$, $R_{o,H} = 0.92$, and $R_{o,V} = 0.93$. Once the weighting factor η_p and the brightness temperatures of the surrounding area $TB_{O,p}$ are known, the brightness temperatures emitted from the observed soil–vegetation scene $TB_{S,p}$ can be derived from the L-band radiometer measurements using Equation (1).

The brightness temperatures emitted from the soil–vegetation scene ($TB_{S,p}$) were simulated using a simple radiative transfer (RT) model, referred to as the tau-omega (τ-ω) model [15], which describes

the emission contributions of soil and vegetation. The τ-ω model is a zero-order solution of the radiative transfer equations:

$$TB_{S,p} = (1 - \omega_p)\,(1 - \gamma_p)\,T_C + (1 - \omega_p)\,(1 - \gamma_p)\,\gamma_p\,R_p\,T_C + (1 - R_p)\,\gamma_p\,T_G, \quad (5)$$

where T_G (K) and T_C (K) are the effective soil and vegetation temperatures, respectively; R_p is the soil surface reflectivity; ω_p is the effective scattering albedo, which accounts for scattering effects within the vegetation canopy [25]; and γ_p is the vegetation transmissivity, computed from the vegetation opacity or optical depth τ_p as follows:

$$\gamma_p = \exp\left(-\frac{\tau_p}{\cos(\theta)}\right), \quad (6)$$

where θ (rad) is the incidence angle.

Soil surface roughness was accounted for in the modelling of the radiometer data by using the semi-empirical approach of Wang and Choudhury [26], which can be described as follows:

$$R_p = [(1 - Q_R)\,R_p^* + Q_R\,R_q^*]\,\exp[-H_R\,\cos(\theta)^{N_R}], \quad (7)$$

where R_p is the rough soil surface reflectivity and R_p* is the specular reflectivity, q is the opposite polarization of p, Q_R is the polarization mixing parameter (Q_R = 0 as polarization crosstalk is assumed to be negligible [11,27]), N_R expresses the angular dependence of roughness (N_R = −1 as proposed in [11,27,28]), and H_R accounts for the intensity of the roughness effect.

The soil surface roughness was considered as constant during the experiment. The value of the H_R parameter can be obtained by inverting the $TB_{S,p}$ data derived from the measurements collected during the layer experiment for the setup configuration with the soil without the vegetation (Step 2 in Figure 4, 10 measurements × 2 polarizations). In that case, only the soil parameters have to be retrieved, i.e., ε_r and H_R, because only the soil contributed to the measured $TB_{S,p}$. To better constrain the inversion, ε_r was estimated from the in situ measurements.

The vegetation effective scattering albedo parameter ω_p was considered as unknown. It was also assumed to be polarization dependent ($\omega_H \neq \omega_V$) and constant over time as the vegetation structure did not significantly change during the experiment.

The vegetation optical depth parameter τ_p was considered as unknown but independent of polarization ($\tau_H = \tau_V = \tau$) and varying over time to follow the time changes of the vegetation water content during the experiment.

The soil relative dielectric permittivity ε_r and the vegetation parameters, i.e., ω_H, ω_V and τ, were then retrieved through inverse modelling. To limit the number of parameters to be retrieved simultaneously as only two $TB_{S,p}$ data ($TB_{S,H}$ and $TB_{S,V}$) were available for each time step (i.e., every 15 min), a two-step inversion approach was used. Values of the parameters ω_H and ω_V were first assumed to be in the range 0–0.2 as proposed in [12]. For each possible combination of ω_H and ω_V in that range (i.e., 21 × 21 combinations considering a step of 0.01 for the ω values), only τ and ε_r were derived for all time steps. Optimal parameter values can then be obtained after finding the minimum of the objective function ϕ (minimum of the sum of the squared difference between the measured and modelled $TB_{S,p}$) between the 21 × 21 inversion runs. All optimizations were performed using the global multilevel coordinate search (GMCS) algorithm as introduced by Huyer and Neumaier [29].

Another approach to estimating ω_H and ω_V separately is to analyse the layer experiment data for the setup configuration with the vegetation shielded from the soil by a grid (Step 5 in Figure 4). In this case, only the vegetation parameters have to be retrieved, i.e., ω_H, ω_V, and τ, because only the vegetation layer contributes to the measured $TB_{S,p}$. The system can also be considered as stable during the radiometer measurements because of the short duration of the experiment (~30 min). More than 3 observations (10 measurements × 2 polarizations) are then available to retrieve the three parameters. Unfortunately, inconsistent parameter values were obtained by this method. This could be explained

by a non-adequate setup (difficulty in properly placing the grid just below the vegetation layer without damaging the vegetation), which did not allow accurate measurement of the radiation originating from the vegetation layer only.

To reduce the noise observed in the $TB_{S,p}$ data, a sliding window of five measurements was applied to the whole dataset. Data before, during, and directly after the irrigation were not considered either in the inversion process to limit the complexity of the interpretation of the results.

2.4. Ground-Penetrating Radar Measurements of Soil Surface Roughness

Ground-penetrating radar (GPR) measurements were also performed to characterize the surface roughness of the organic soils. In particular, GPR measurements were performed when the vegetation layer was completely removed (Step 2 of the layer experiment, see Figure 4) in order to avoid any effect of the vegetation on the GPR signal.

The GPR system, operating in the frequency domain, consisted of an ultrawideband stepped-frequency continuous-wave radar connected to a monostatic doubled-ridge horn antenna (BBHA 9120 A, Schwarzbeck Mess-Elektronik, Schönau, Germany) with 14 cm × 25 cm aperture area and 22 cm height (Figure 5). The antenna nominal frequency range is 0.8–5.2 GHz and its isotropic gain ranges from 4.4 to 14.0 dBi. The antenna was connected to the reflection port of a vector network analyser (VNA, ZVL, Rohde & Schwarz, Munich, Germany) and situated at an average height of 40 cm above the soil surface with a normal incidence. Measurements were performed with a frequency step of 4 MHz. Before each set of measurement, the VNA was calibrated at the connection between the coaxial cable and the antenna using a standard open-short-match calibration kit.

Figure 5. Pictures of the off-ground ground-penetrating radar (GPR) system fixed above the organic soils (with the vegetation layer removed) consisting of a vector network analyser connected to a horn antenna with a low-loss N-type 50 Ω impedance coaxial cable.

The radar data can be described using the antenna-medium model developed by Lambot et al. [30]. In this model, the far-field radar antenna is modelled using frequency-dependent global reflection and transmission coefficients and Green functions are used to model the frequency response of the soil medium. Soil surface roughness was accounted for in the modelling of the GPR data using the approach proposed by Jonard et al. [31].

Soil relative dielectric permittivity (ε_r) and soil surface roughness, i.e., the standard deviation of the surface height (σ_R, m) can be retrieved through inverse modelling in the time domain by focusing on a time window containing the surface reflection only. To better constrain the inversion of σ_R, ε_r was estimated from the in situ measurements as for the estimation of the soil roughness from radiometer data (see above). In addition, inversion of the data was performed in a limited frequency band, between 0.8 GHz and 2.2 GHz, and with a central frequency close to that of the ELBARA II radiometer.

2.5. Laboratory Measurements of Vegetation and Soil Water Content

Vegetation and soil (organic and mineral layers) water content were determined using the oven drying method. For the soil samples, we used a drying temperature of 85 °C for a period of 48 h. This temperature was used in order to avoid charring of the organic fraction, which may occur at the standard drying temperature of 105 °C [32]. The vegetation samples were dried at 60 °C for a period of 48 h.

2.6. Meteorological Data

Meteorological data, in particular, air temperature, precipitation, and wind speed, were monitored with an automatic meteorological station installed on the test site at about 35 m from the organic soils (data publicly available on the TERENO data portal: http://teodoor.icg.kfa-juelich.de/ibg3searchportal2/index.jsp).

3. Results

3.1. L-Band Brightness Temperature Measurements

Figure 6a shows the time-lapse brightness temperature (TB_S) measurements at H and V polarization. In addition to the small diurnal variations, we observed a significant increase in TB_S at both polarizations after the irrigation event (DOY 281) and a general decrease from DOY 288 to the end of the experiment (DOY 330). In general, a decrease in $TB_{S,p}$ is expected after irrigation due to an increase in soil water content. However, in this case, the increase in $TB_{S,p}$ observed on DOY 281 is explained by an increase in vegetation water content (see Figure 6d) and also in the amount of intercepted water by the vegetation due to the irrigation [33], relatively larger than the increase in soil water content. On the contrary, the observed decrease in $TB_{S,p}$ from DOY 288 to DOY 330 is explained by the combined effects of an increase mainly in soil permittivity/water content due to the repetitive rain events during this period and a general decrease in air and soil temperature (see Figure 6c). Indeed, at microwave frequencies, the emitted radiance $TB_{S,p}$ is linearly related to the effective physical temperature and to the emissivity of the observed scene, the latter being inversely proportional to the effective permittivity of the scene (Rayleigh–Jeans law).

As can be seen in Figure 7, about 139 mm of precipitation were recorded over the measurement period with a relative homogeneous distribution over time. The largest rain event was observed on DOY 311 with a total rainfall of 14.1 mm.

During the experiment (from DOY 276 to DOY 330), $TB_{S,H}$ ranged between 226.3 and 245.8 K, while $TB_{S,V}$ was always above $TB_{S,H}$ with values ranging from 237.3 to 253.3 K. Missing data (from DOY 290.5 to DOY 291.7; DOY 301.4 to DOY 304.0; DOY 316.5 to DOY 317.5; DOY 318.4 to DOY 319.6; and DOY 323.5 to DOY 324.7) are due to instrument failures or filtering of inconsistent data, in particular, during heavy wind events (leading to an incorrect azimuthal orientation of the antenna).

3.2. In Situ Measurements

The soil relative dielectric permittivity measured by the in situ sensors progressively increased over time, from 9.8 and 10.8 at 3 and 10 cm depth respectively at the beginning of the experiment to 29.2 and 22.9 at the end of the experiment (Figure 6b). At DOY 281, a significant jump can be observed after the irrigation with high values in particular for the near-surface measurements (up to 42.8). In addition to the general increasing trend, small diurnal variations can be observed. The soil permittivity values were systematically higher at 3 cm than at 10 cm depth.

The air temperature (T_{air}) measurements collected from the meteorological station ranged from −1.0 (DOY 320) to 24.2 °C (DOY 292) with large daily variations (Figure 6c). A drop in air temperature was observed around DOY 285 as well as a general decrease from DOY 292 to the end of the experiment. Slightly negative air temperature values occurred only on DOY 320. Soil temperature (T_G) values were similar at the two investigated depths, ranging from 5.1 (DOY 281) to 15.7 °C (DOY 330) during the

experiment. The general trend of the soil temperatures is similar to that of air temperature but with smaller diurnal variations.

The gravimetric vegetation water content (*VWC*, kg m^{-2}) derived from laboratory measurements ranged from 0.37 (DOY 281) to 2.3 kg m^{-2} (DOY 323) with a significant increase after the irrigation followed by a large drop and a second increase from DOY 295 to DOY 323 (Figure 6d). However, only nine *VWC* measurements were performed during the experiment due to time and technical constraints, with the larger data gap between DOY 304 and DOY 323.

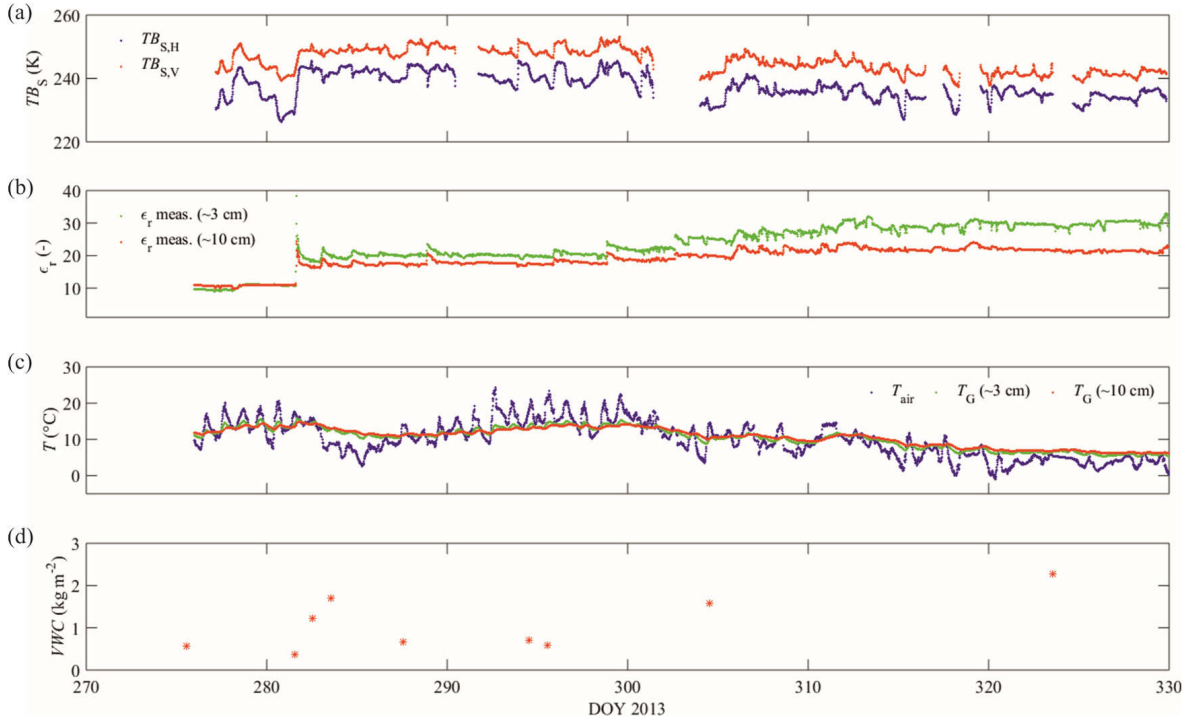

Figure 6. (**a**) ELBARA brightness temperature (TB_S) at horizontal (blue dots) and vertical (red dots) polarizations as a function of day of the year (DOY) over fifty-four days and with a measurement interval of 15 min; (**b**) soil relative dielectric permittivity (ε_r) measured by the 5TE sensors at 3 and 10 cm depth; (**c**) soil temperature (T_G) measured by the 5TE sensors at 3 and 10 cm depth and air temperature (T_{air}) measured at the meteorological station; and (**d**) gravimetric vegetation water content (*VWC*) derived from laboratory measurements on vegetation samples.

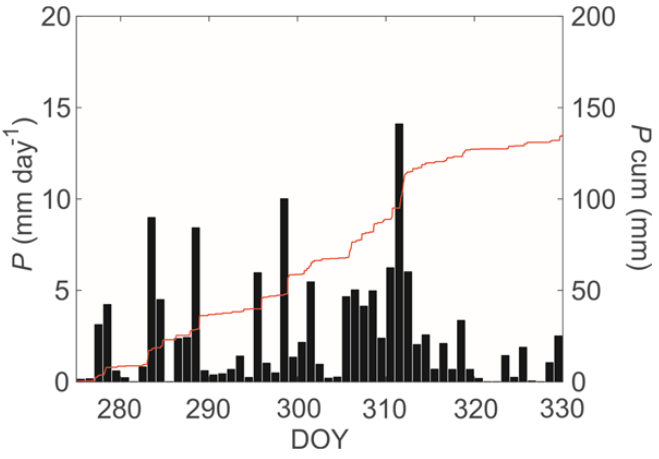

Figure 7. Daily (P, mm day^{-1}) and cumulative (P_{cum}, mm) precipitation measured at the test site.

3.3. Inversion of L-Band Brightness Temperature Data

Modelled and measured $TB_{S,p}$ data are shown in Figure 8a. The modelled radiometer data agree perfectly with the observations (r = 1 and RMSE = 2×10^{-10}), which confirm that the RT model with the retrieved soil and vegetation parameters can accurately reproduce the observed data.

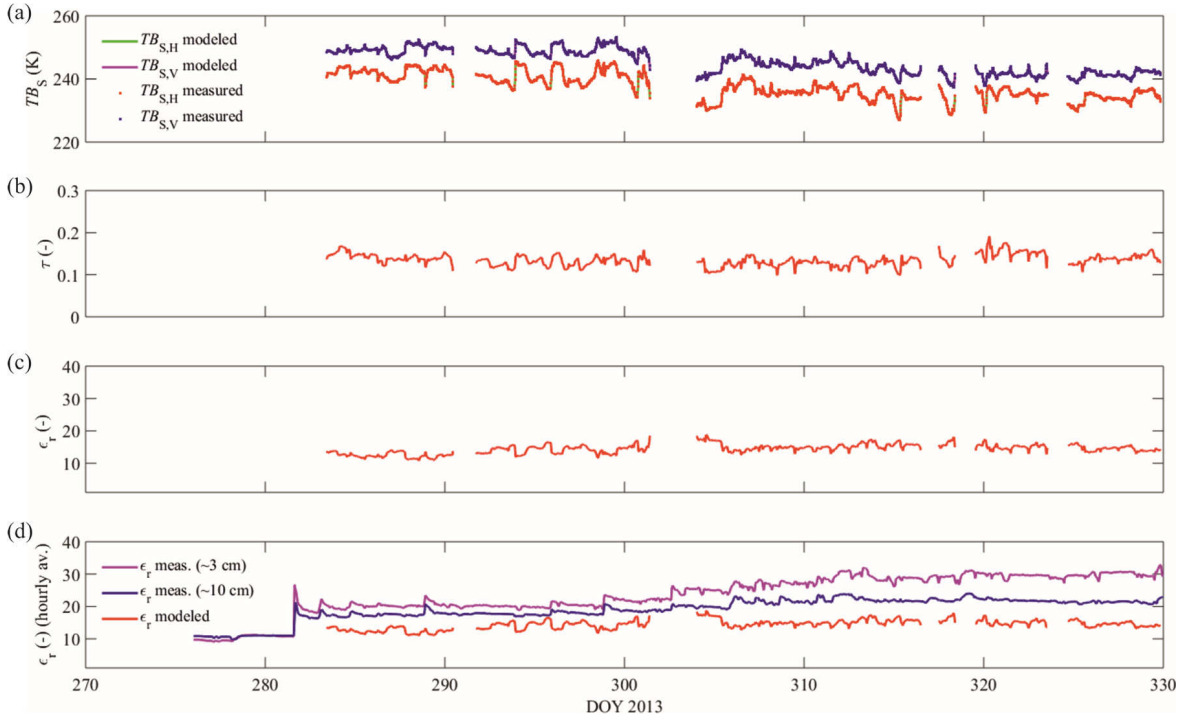

Figure 8. (**a**) Measured (blue and red dots) and modelled (green and magenta lines) L-band brightness temperatures (TB_S) at horizontal and vertical polarizations. Modelled $TB_{S,p}$ data were obtained using the τ-ω radiative transfer model. It should be noted that the modelled data can hardly be seen on the plot because of the perfect agreement between the measured and modelled data. (**b**) Vegetation optical depth (τ); and (**c**) soil relative dielectric permittivity (ε_r) derived from $TB_{S,p}$ data. (**d**) Comparison of hourly mean radiometer-derived ε_r with in situ ε_r measurements at 3 and 10 cm depth.

3.3.1. Soil Roughness Parameter

Inversion for the soil roughness parameter H_R from 10 radiometer measurements above the soil-only setup (Step 2 of the layer experiment, see Figure 4) gave a value of 0.49, which corresponds to a standard deviation of the surface height σ_R of 0.012 m based on the formulation proposed by Choudhury et al. [34] or a σ_R of 0.013 m if we used the formulation of Wigneron et al. [12]. It should be noted that the inversion was performed in a large parameter space ($0 < H_R < 1$), which ensured finding the global optimum.

In addition, GPR measurements were performed above the same soil-only setup in order to have an additional estimation of the soil surface roughness. Figure 9 depicts the measured Green's function (computed from the radar data S_{11} using the antenna-medium model [30]) in the time domain. The soil surface reflection can be clearly observed between 3 and 4 ns. The modelled Green's function fits almost perfectly the measured Green's function at the surface reflection, which means that the GPR model was able to capture and accurately reproduce the soil surface reflection. The estimated value of σ_R derived from the GPR data is 0.013 m, which is in a perfect agreement with the soil surface roughness estimation from radiometer data.

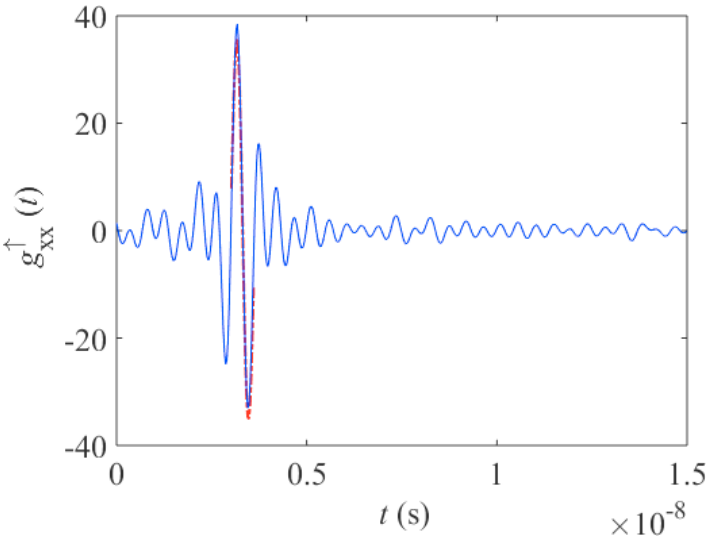

Figure 9. Measured (solid blue line) and modelled (dash-dotted red line) radar Green's function ($g_{xx}^{\uparrow}$) in the time (t)-domain.

3.3.2. Effective Vegetation Scattering Albedo and Vegetation Optical Depth

Based on the two-step inversion approach, the optimal values obtained for the effective vegetation scattering albedo parameter ω_p are $\omega_H = 0.01$ and $\omega_V = 0.19$. Figure 8b shows the estimated vegetation optical depth (τ) values over time. The inversion was performed in the parameter space $0 < \tau < 0.6$. The τ values obtained oscillate between 0.10 and 0.19 with a mean value of 0.13. The time variations in the estimated τ shown in Figure 8b can be explained by the combined effect of changes in vegetation water content, changes in water content of the layer litter, and changes in the amount of water intercepted by the vegetation after rainfall or dew events during the experiment.

3.3.3. Soil Relative Dielectric Permittivity

The estimated values of the soil relative dielectric permittivity ε_r are shown in Figure 8c. The inversion was also performed in a large parameter space ($1 < \varepsilon_r < 40$). The optimized ε_r values oscillate between 10.80 and 18.82 with a mean value of 14.39. As shown in Figure 8d, the radiometer-derived ε_r values are significantly lower compared to the in situ measurements. The corresponding scatter plots between modelled and in situ ε_r and the regression lines are shown in Figure 10. As can be seen in the scatter plots, a data cloud is detectable. However, the correlations between the modelled and measured ε_r are significant with correlation coefficients (r) of 0.50 (p-value < 0.0001) and 0.49 (p-value < 0.0001) for the measurements at 3 and 10 cm depth, respectively (see Table 1). It should be noted that the correlation coefficients were obtained using the robust least absolute residual (LAR) method, which has the advantage of being more outlier-resistant than the classically used least square fitting approach. On the other hand, the slopes and intercepts of the regression lines (see Table 1) indicate a clear offset between the measured and modelled ε_r, whereby the modelled ε_r are always smaller than the measured ones. Furthermore, a better agreement is systematically observed between the modelled ε_r and the in situ ε_r measurements at 10 cm depth compared to the in situ measurements at 3 cm depth. This is also reflected in the calculated bias of -10.74 and -5.63 and the unbiased root-mean-square error (ubRMSE) of 3.77 and 1.84, at 3 and 10 cm depth, respectively (Table 1).

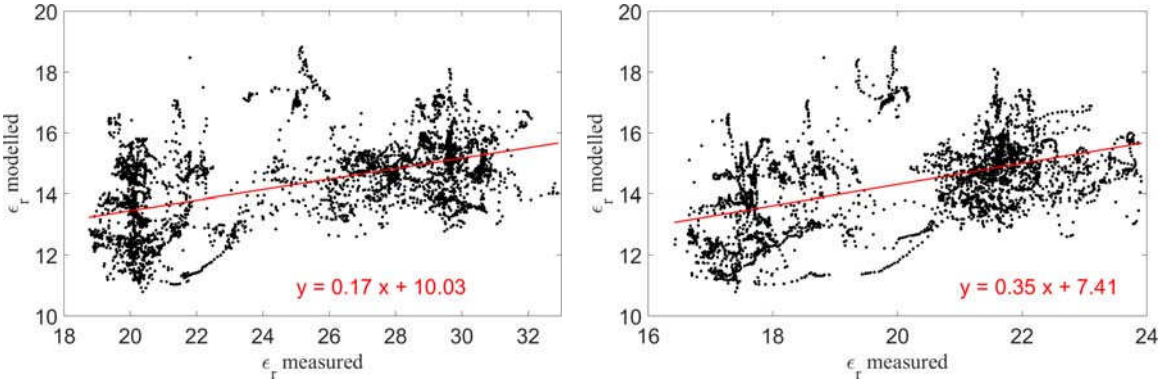

Figure 10. Comparison of the soil relative dielectric permittivities (ε_r) derived from the radiometer measurements with the in situ ε_r measurements at: 3 cm depth (**left**); and 10 cm depth (**right**). Regression lines are based on the robust least absolute residual (LAR) method and their equation are shown in red.

Table 1. Parameter estimates (*a* and *b*) and correlation coefficient (r) of the regression lines between the measured and modelled soil relative dielectric permittivities (ε_r) based on the robust least absolute residual (LAR) method. Confidence intervals (95%) are presented in parentheses. Bias and unbiased root-mean-square error (ubRMSE) between measured and modelled ε_r are also shown.

	3 cm Depth	10 cm Depth
a [1]	0.17 (0.16, 0.18)	0.35 (0.33, 0.36)
b [1]	10.03 (9.79, 10.27)	7.41 (7.01, 7.80)
r	0.50	0.49
bias	−10.74	−5.63
ubRMSE	3.77	1.84

[1] $y = a\,x + b$ (with y = modelled ε_r and x = measured ε_r).

3.4. Response Surface Analysis

Response surfaces were calculated to analyse the uniqueness of the inverse solution as well as the parameter sensitivities and the correlations between the parameters of the RT model. Figure 11 shows the response surfaces of the objective function ϕ in the ε_r-ω_V, τ-ω_V, ε_r-H_R, τ-H_R, ε_r-τ, and ω_H-ω_V parameter planes. These response surfaces were calculated considering data with intermediate soil dielectric permittivity and optical depth values (i.e., $\varepsilon_r = 14.49$ and $\tau = 0.146$ inverted from $TB_{S,H} = 234.8$ and $TB_{S,V} = 241.8$ observed on DOY 307), but similar results were obtained for the other conditions observed during the experiment. Inversions were performed in a large parameter space ($1 < \varepsilon_r < 40$; $0 < H_R < 1$; $0 < \tau < 0.6$; $0 < \omega_V < 0.25$) and the range of each parameter was divided into 200 discrete values resulting in 40,000 objective function values for each contour plot. For each response surface, no local minima can be observed in addition to the global minimum. In the ε_r-H_R parameter plane, the global minimum region suggests a significant positive correlation between the two parameters (Figure 11c). A similar signal can indeed be obtained for either a low dielectric permittivity with a low roughness amplitude, or a high dielectric permittivity with a high roughness amplitude. On the contrary, the τ-H_R response surface indicates a negative correlation between τ and H_R (Figure 11d). An accurate estimation of ε_r and/or τ is therefore not possible without a priori information about H_R. The ε_r-ω_V and τ-ω_V response surfaces show an elliptical global minimum region parallel to the ω_V axis, which suggest that the two parameter pairs are uncorrelated (Figure 11a,b). In addition, these two plots indicate that the RT model is less sensitive to ω_V than to ε_r, and τ. Similar plots were obtained when considering ω_H instead of ω_V (not shown). For the ε_r-τ response surface, a positive correlation between the two parameters can be observed, which increase parameter estimation uncertainty when both parameters are retrieved simultaneously (Figure 11e). Finally, no correlation can be observed

between ω_H and ω_V from the ω_H-ω_V response surface (Figure 11f). Moreover, the global minimum is very well-defined in this case.

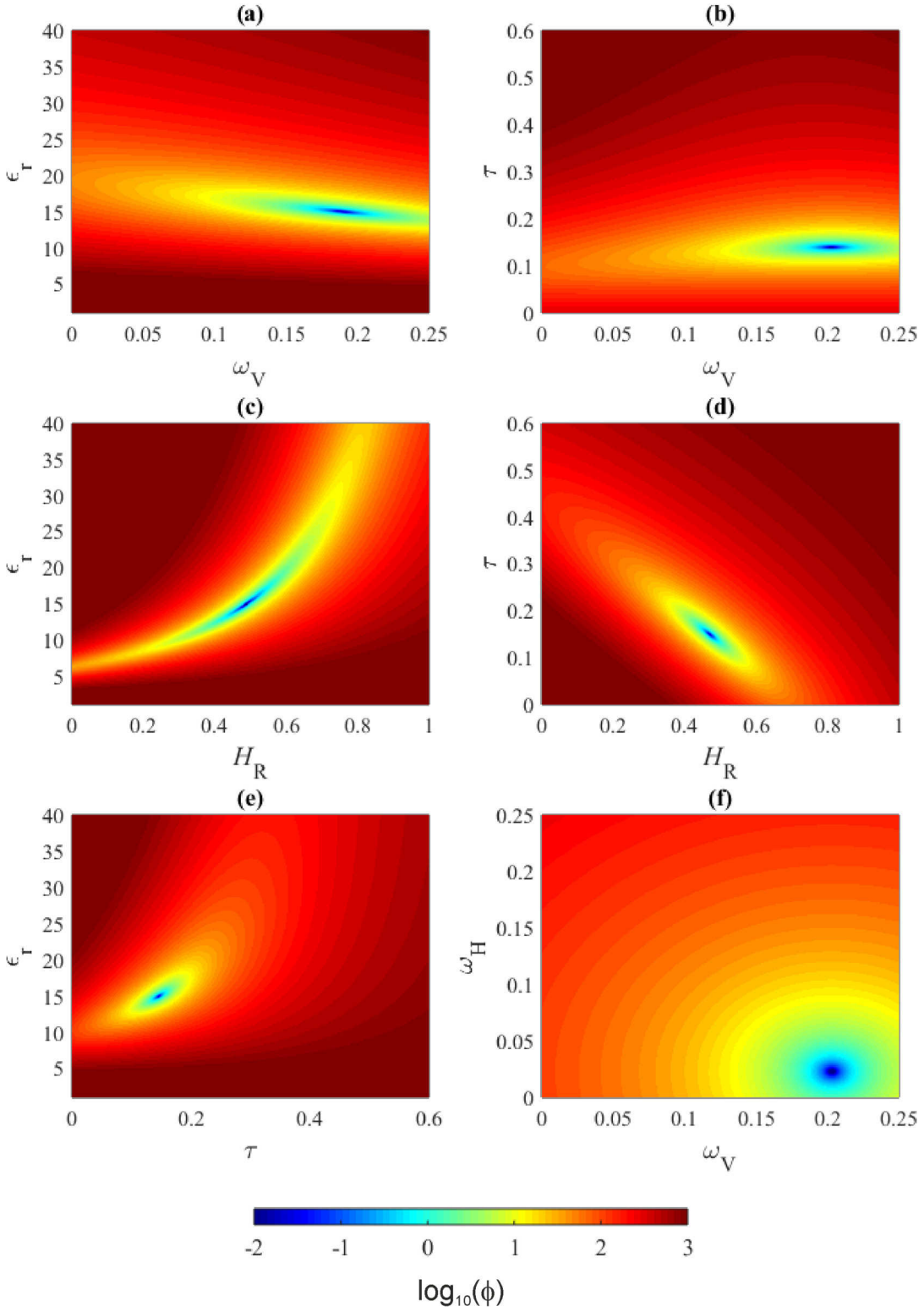

Figure 11. Response surfaces of the logarithm of the objective function ($\log_{10}(\phi)$) in the following parameter planes: ε_r-ω_V (**a**); τ-ω_V (**b**); ε_r-H_R (**c**); τ-H_R (**d**); ε_r-τ (**e**); and ω_H-ω_V (**f**).

4. Discussion

4.1. Soil Roughness and Effective Vegetation Scattering Albedo Parameters

In this study, the roughness parameter H_R was first estimated based on a specific setup and using in situ dielectric permittivity measurements. The retrieved value for H_R is 0.49, which is close to the H_R value of 0.4 derived in [27] based on a globally-constant calibration of the soil roughness and effective scattering albedo parameters from SMOS data. The estimated value for H_R was also confirmed by the estimation from the GPR measurements performed above the same setup in a similar frequency range. The relatively high value obtained in this study for H_R might be explained by the large heterogeneity of the litter and the organic soil surface layer. However, the retrieved value differs significantly from the value of 0.1 and 0.156 used for areas covered by low vegetation in the operational SMOS and SMAP Level 3 soil moisture algorithms (namely SMOSL3 and SMAP_SCA). As shown in Figure 11c,d, H_R is significantly correlated to ε_r and τ and can therefore not be retrieved simultaneously with these two parameters. This means that H_R has to be calibrated first as done in our study or set a priori as done in SMOSL3 and SMAP_SCA. As can also be seen from the response surfaces, using a H_R value specifically calibrated for organic soils instead of a default value of 0.1 (SMOSL3) or 0.156 (SMAP_SCA) might lead to a significant improvement in soil dielectric permittivity and optical depth retrievals over areas dominated by organic soils.

The aim of this study was also to test the dependency on polarization of the effective vegetation scattering albedo ω_p. The results indicate a clear dependency on polarization of ω_p, which reflects the significant impact of the vegetation architecture on the scattering of the L-band radiation. In addition, the value of ω_H close to 0 indicates that the scattering effects across the vegetation can be neglected at H polarization, while the high value for ω_V (i.e., 0.19) indicates that the scattering effects are important at V polarization. Figure 11f clearly shows that the ω_H and ω_V parameters are uncorrelated and can thus be retrieved simultaneously during the inversion process. This dependency on polarization was also observed by Saleh et al. [35] over grass with $\omega_H = 0$ and ω_V between 0.05 and 0.2 depending on grass type as well as by Kurum et al. [25] for corn and soybean canopies. The results obtained in this study showed that the assumption of a polarization independent ω currently used for the operational SMOSL3 ($\omega_H = \omega_V = 0$) and SMAP_SCA ($\omega_H = \omega_V = 0.05$) algorithms is not valid and could lead to inaccuracy in the soil dielectric permittivity/water content and vegetation optical depth retrievals, while the sensitivity of the RT model to ω_V is relatively low (see Figure 11a,b).

4.2. Soil Relative Dielectric Permittivity Retrieval

The results of the inversion of the $TB_{S,p}$ data show that the radiometer-derived ε_r are significantly correlated with the in situ measurements, but their values are systematically lower compared to the in situ ones (Figure 8d). The lower values obtained for the modelled compared to the in situ ε_r could be explained by the difference between the operating frequency of the radiometer (1.4 GHz) and that of the 5TE sensors (70 MHz). Bobrov et al. [36] found that the dielectric permittivity of soils in the frequency range from 10 MHz to 1 GHz increased with decreasing frequency and increasing soil water content. In addition, the largest variations with increasing frequency were observed under high clay and organic matter contents. Kelleners et al. [37] also observed in dispersive clay soils a frequency dependence of the dielectric permittivity below 500 MHz with lower values of dielectric permittivity at higher frequencies as observed in the current study (see also [38]). Similar effects might indeed be expected in organic soils as in clay soils, as the organic constituents have also large specific areas with high surface charges. In addition, because of the positive correlation between ε_r and τ observed in Figure 11e, some uncertainty in the estimation of these two parameters can be expected when both parameters are retrieved simultaneously.

5. Conclusions

We experimentally carried out retrievals of electromagnetic and hydrological characteristics of organic soil surface layers using ground-based L-band radiometry data. To this end, undisturbed organic soil blocks with their vegetation cover were collected from a heathland in the Skjern River catchment in western Denmark. The soil structure was then reconstituted at the Selhausen remote sensing field laboratory in Germany, which made it possible to perform L-band radiometer measurements of the soils over a period of two months. Time-lapse brightness temperature data were inverted using the tau-omega (τ-ω) RT model for estimating the time variations in the soil relative dielectric permittivity and the vegetation optical depth. In addition, the effective vegetation scattering albedo parameter of the RT model was retrieved based on a two-step inversion approach. The remote estimations of the relative dielectric permittivity were finally compared to in situ measurements at 3 and 10 cm depth.

The results indicated that the radiometer-derived dielectric permittivities were significantly correlated with the in situ measurements, but that their values were systematically lower compared to the in situ ones (bias = −10.74, ubRMSE = 3.77 for the in situ measurements at 3 cm depth; and bias = −5.63, ubRMSE = 1.84 for the in situ measurements at 10 cm depth). This could be explained by the frequency dependence of the soil dielectric permittivity at low frequency (70 MHz) in organic rich soils. The effective vegetation scattering albedo parameter was found to be polarization dependent. While the scattering effect within the vegetation could be neglected at horizontal polarization (ω_H = 0.01), it was found to be important at vertical polarization (ω_V = 0.19). The vegetation optical depth estimated values over time oscillated between 0.10 and 0.19 with a mean value of 0.13.

These results should be confirmed and extended in future by conducting additional tower-based experiments with passive but also active L-band microwave sensors and with different soil types exhibiting a range of organic matter content and moisture content. There is also room for improvement by considering more advanced RT models accounting for a multi-layered soil medium instead of the widely used τ-ω model, which considers the soil as a homogeneous medium. This would make it possible to take account of the effect of the under-laying mineral soil layer and the effect of a vertical gradient of organic matter content in the organic soil surface layer.

Finally, this study provides a further contribution to the characterization of the L-band emissions of organic soil surface layers, which might be used to improve the quality of space-borne remote sensing soil moisture data acquired over areas dominated by organic soils.

Acknowledgments: The ELBARA-II radiometer was provided by the Terrestrial Environmental Observatories (TERENO) initiative funded by the Helmholtz Association of German Research Centres. The organic soils collected from the Gludsted heathland, Denmark, were excavated and provided by HOBE (Hydrological Observatory). Simone Bircher was funded by the ESA SMOSHiLat project (Changing Earth Science Network) and by ExpeER (Experimentation in Ecosystem Research).

Author Contributions: François Jonard, Simone Bircher, François Demontoux, Lutz Weihermüller and Stephen Razafindratsima conceived and designed the experiments; François Jonard, Simone Bircher and Lutz Weihermüller performed the experiments; François Jonard analysed the data; François Jonard, Simone Bircher, Jean-Pierre Wigneron and Harry Vereecken provided scientific expertise; and François Jonard wrote the paper.

Conflicts of Interest: The authors declare no conflict of interest.

References

1. Stokstad, E. Defrosting the carbon freezer of the north. *Science* **2004**, *304*, 1618–1620. [CrossRef] [PubMed]
2. Schuur, E.A.G.; Bockheim, J.; Canadell, J.G.; Euskirchen, E.; Field, C.B.; Goryachkin, S.V.; Hagemann, S.; Kuhry, P.; Lafleur, P.M.; Lee, H.; et al. Vulnerability of permafrost carbon to climate change: Implications for the global carbon cycle. *Bioscience* **2008**, *58*, 701–714. [CrossRef]
3. Schuur, E.A.G.; Abbott, B.; Permafrost Carbon, N. High risk of permafrost thaw. *Nature* **2011**, *480*, 32–33. [CrossRef] [PubMed]

4. Davidson, E.A.; Janssens, I.A. Temperature sensitivity of soil carbon decomposition and feedbacks to climate change. *Nature* **2006**, *440*, 165–173. [CrossRef] [PubMed]
5. Shi, J.C.; Du, Y.; Du, J.Y.; Jiang, L.M.; Chai, L.N.; Mao, K.B.; Xu, P.; Ni, W.J.; Xiong, C.; Liu, Q.; et al. Progresses on microwave remote sensing of land surface parameters. *Sci. China Earth Sci.* **2012**, *55*, 1052–1078. [CrossRef]
6. Kerr, Y.H.; Waldteufel, P.; Wigneron, J.P.; Delwart, S.; Cabot, F.; Boutin, J.; Escorihuela, M.J.; Font, J.; Reul, N.; Gruhier, C.; et al. The SMOS mission: New Tool for Monitoring Key Elements of the Global Water Cycle. *Proc. IEEE* **2010**, *98*, 666–687. [CrossRef]
7. Le Vine, D.M.; Dinnat, E.P.; Meissner, T.; Yueh, S.H.; Wentz, F.J.; Torrusio, S.E.; Lagerloef, G. Status of Aquarius/SAC-D and Aquarius Salinity Retrievals. *IEEE J. Sel. Top. Appl. Earth Obs. Remote Sens.* **2015**, *8*, 5401–5415. [CrossRef]
8. Entekhabi, D.; Njoku, E.G.; O'Neill, P.E.; Kellogg, K.H.; Crow, W.T.; Edelstein, W.N.; Entin, J.K.; Goodman, S.D.; Jackson, T.J.; Johnson, J.; et al. The Soil Moisture Active Passive (SMAP) Mission. *Proc. IEEE* **2010**, *98*, 704–716. [CrossRef]
9. Konings, A.G.; Piles, M.; Das, N.; Entekhabi, D. L-band vegetation optical depth and effective scattering albedo estimation from SMAP. *Remote Sens. Environ.* **2017**, *198*, 460–470. [CrossRef]
10. Vereecken, H.; Weihermüller, L.; Jonard, F.; Montzka, C. Characterization of crop canopies and water stress related phenomena using microwave remote sensing methods: A review. *Vadose Zone J.* **2012**, *11*. [CrossRef]
11. Parrens, M.; Wigneron, J.-P.; Richaume, P.; Mialon, A.; Al Bitar, A.; Fernandez-Moran, R.; Al-Yaari, A.; Kerr, Y.H. Global-scale surface roughness effects at L-band as estimated from SMOS observations. *Remote Sens. Environ.* **2016**, *181*, 122–136. [CrossRef]
12. Wigneron, J.P.; Jackson, T.J.; O'Neill, P.; De Lannoy, G.; de Rosnay, P.; Walker, J.P.; Ferrazzoli, P.; Mironov, V.; Bircher, S.; Grant, J.P.; et al. Modelling the passive microwave signature from land surfaces: A review of recent results and application to the L-band SMOS & SMAP soil moisture retrieval algorithms. *Remote Sens. Environ.* **2017**, *192*, 238–262.
13. Bircher, S.; Kerr, Y.H.; Wigneron, J.-P. SMOSHiLat—Microwave L-Band Emissions from Organic-Rich Soils in the Northern Cold Climate Zone and Their Impact on the SMOS Soil Moisture Product. In *Support to Science Element—Changing Earth Science Network*; ESA-ESRIN: Frascati, Italy, 2015; p. 71.
14. Mätzler, C. *Thermal Microwave Radiation: Applications for Remote Sensing*; The Institution of Engeneering and Technology: London, UK, 2006; p. 544.
15. Mo, T.; Choudhury, B.J.; Schmugge, T.J.; Wang, J.R.; Jackson, T.J. A model for microwave emission from vegetation-covered fields. *J. Geophys. Res.* **1982**, *87*, 11229–11237. [CrossRef]
16. Dobson, M.C.; Ulaby, F.F.; Hallikainen, M.T.; El-Rayes, M.A. Microwave dielectric behavior of wet soil—Part II: Dielectric mixing models. *IEEE Trans. Geosci. Remote Sens.* **1985**, *23*, 35–46. [CrossRef]
17. Mironov, V.L.; Kosolapova, L.G.; Fomin, S.V. Physically and Mineralogically Based Spectroscopic Dielectric Model for Moist Soils. *IEEE Trans. Geosci. Remote Sens.* **2009**, *47*, 2059–2070. [CrossRef]
18. Wang, J.R.; Schmugge, T.J. An empirical-model for the complex dielectric permittivity of soils as a function of water-content. *IEEE Trans. Geosci. Remote Sens.* **1980**, *18*, 288–295. [CrossRef]
19. Bircher, S.; Demontoux, F.; Razafindratsima, S.; Zakharova, E.; Drusch, M.; Wigneron, J.P.; Kerr, Y.H. L-Band Relative Permittivity of Organic Soil Surface Layers—A New Dataset of Resonant Cavity Measurements and Model Evaluation. *Remote Sens.* **2016**, *8*, 17. [CrossRef]
20. Jin, M.; Zheng, X.; Jiang, T.; Li, X.; Li, X.-J.; Zhao, K. Evaluation and Improvement of SMOS and SMAP Soil Moisture Products for Soils with High Organic Matter over a Forested Area in Northeast China. *Remote Sens.* **2017**, *9*, 387. [CrossRef]
21. Mironov, V.; Savin, I. A temperature-dependent multi-relaxation spectroscopic dielectric model for thawed and frozen organic soil at 0.05–15 GHz. *Phys. Chem. Earth* **2015**, *83–84*, 57–64. [CrossRef]
22. Mironov, V.L.; Kerr, Y.H.; Kosolapova, L.G.; Savin, I.V.; Muzalevskiy, K.V. A Temperature-Dependent Dielectric Model for Thawed and Frozen Organic Soil at 1.4 GHz. *IEEE J. Sel. Top. Appl. Earth Obs. Remote Sens.* **2015**, *8*, 4470–4477. [CrossRef]
23. Jonard, F.; Weihermüller, L.; Schwank, M.; Jadoon, K.Z.; Vereecken, H.; Lambot, S. Estimation of hydraulic properties of a sandy soil using ground-based active and passive microwave remote sensing. *IEEE Trans. Geosci. Remote Sens.* **2015**, *53*, 3095–3109. [CrossRef]

24. Bircher, S.; Andreasen, M.; Vuollet, J.; Vehviläinen, J.; Rautiainen, K.; Jonard, F.; Weihermüller, L.; Zakharova, E.; Wigneron, J.P. Soil moisture sensor calibration for organic soil surface layers. *Geosci. Instrum. Methods Data Syst.* **2016**, *5*, 109–125. [CrossRef]
25. Kurum, M. Quantifying scattering albedo in microwave emission of vegetated terrain. *Remote Sens. Environ.* **2013**, *129*, 66–74. [CrossRef]
26. Wang, J.R.; Choudhury, B.J. Remote-sensing of soil-moisture content over bare field at 1.4 GHz frequency. *J. Geophys. Res.* **1981**, *86*, 5277–5282. [CrossRef]
27. Fernandez-Moran, R.; Wigneron, J.P.; De Lannoy, G.; Lopez-Baeza, E.; Parrens, M.; Mialon, A.; Mahmoodi, A.; Al-Yaari, A.; Bircher, S.; Al Bitar, A.; et al. A new calibration of the effective scattering albedo and soil roughness parameters in the SMOS SM retrieval algorithm. *Int. J. Appl. Earth Obs. Geoinf.* **2017**, *62*, 27–38. [CrossRef]
28. Wigneron, J.P.; Kerr, Y.; Waldteufel, P.; Saleh, K.; Escorihuela, M.J.; Richaume, P.; Ferrazzoli, P.; de Rosnay, P.; Gurney, R.; Calvet, J.C.; et al. L-band Microwave Emission of the Biosphere (L-MEB) Model: Description and calibration against experimental data sets over crop fields. *Remote Sens. Environ.* **2007**, *107*, 639–655. [CrossRef]
29. Huyer, W.; Neumaier, A. Global optimization by multilevel coordinate search. *J. Glob. Optim.* **1999**, *14*, 331–355. [CrossRef]
30. Lambot, S.; Slob, E.C.; van den Bosch, I.; Stockbroeckx, B.; Vanclooster, M. Modeling of ground-penetrating radar for accurate characterization of subsurface electric properties. *IEEE Trans. Geosci. Remote Sens.* **2004**, *42*, 2555–2568. [CrossRef]
31. Jonard, F.; Weihermüller, L.; Vereecken, H.; Lambot, S. Accounting for soil surface roughness in the inversion of ultrawideband off-ground GPR signal for soil moisture retrieval. *Geophysics* **2012**, *77*, H1–H7. [CrossRef]
32. O'Kelly, B.C. Accurate determination of moisture content of organic soils using the oven drying method. *Dry. Technol.* **2004**, *22*, 1767–1776. [CrossRef]
33. Saleh, K.; Wigneron, J.P.; de Rosnay, P.; Calvet, J.C.; Escorihuela, M.J.; Kerr, Y.; Waldteufel, P. Impact of rain interception by vegetation and mulch on the L-band emission of natural grass. *Remote Sens. Environ.* **2006**, *101*, 127–139. [CrossRef]
34. Choudhury, B.J.; Schmugge, T.J.; Chang, A.; Newton, R.W. Effect of surface-roughness on the microwave emision from soils. *J. Geophys. Res.* **1979**, *84*, 5699–5706. [CrossRef]
35. Saleh, K.; Wigneron, J.P.; Waldteufel, P.; de Rosnay, P.; Schwank, M.; Calvet, J.C.; Kerr, Y.H. Estimates of surface soil moisture under grass covers using L-band radiometry. *Remote Sens. Environ.* **2007**, *109*, 42–53. [CrossRef]
36. Bobrov, P.P.; Mironov, V.L.; Kondratyeva, O.V.; Repin, A.V. The Effect of Clay and Organic Matter Content on the Dielectric Permittivity of Soils and Grounds at the Frequency Range from 10 MHz to 1 GHz. In Proceedings of the 2010 IEEE International Geoscience and Remote Sensing Symposium, Honolulu, HI, USA, 25–30 July 2010; pp. 4433–4435.
37. Kelleners, T.J.; Robinson, D.A.; Shouse, P.J.; Ayars, J.E.; Skaggs, T.H. Frequency dependence of the complex permittivity and its impact on dielectric sensor calibration in soils. *Soil Sci. Soc. Am. J.* **2005**, *69*, 67–76.
38. Robinson, D.A.; Campbell, C.S.; Hopmans, J.W.; Hornbuckle, B.K.; Jones, S.B.; Knight, R.; Ogden, F.; Selker, J.; Wendroth, O. Soil moisture measurement for ecological and hydrological watershed-scale observatories: A review. *Vadose Zone J.* **2008**, *7*, 358–389. [CrossRef]